

PAPER

[View Article Online](#)
[View Journal](#) | [View Issue](#)

 Cite this: *Energy Environ. Sci.*, 2022, 15, 2029

Direct optical fiber monitor on stress evolution of the sulfur-based cathodes for lithium–sulfur batteries†

 Ziyun Miao,^{‡a} Yanpeng Li,^{‡b} Xiangpeng Xiao,^b Qizhen Sun,^{ID *b} Bin He,^a Xue Chen,^a Yaqi Liao,^a Yi Zhang,^a Lixia Yuan,^a Zhijun Yan,^b Zhen Li^{*a} and Yunhui Huang^{ID *a}

Lithium–sulfur (Li–S) batteries are competitive for next-generation energy storage applications. However, soluble polysulfides cause severe shuttle effect and electrolyte abuse. Solid–solid and quasi-solid conversions are effective to address the problems, but the mechanistic understanding is still incomplete. In particular, the internal stress evolution which is tied closely to the electrode structure evolution, is rarely explored due to lack of appropriate characterization methods. Here, we report *in situ* monitoring of cathode stress evolution in Li–S batteries via optical fiber Bragg grating (FBG) sensors. Stress evolution in three classic mechanisms of Li–S cells including solid–liquid–solid, solid–solid and quasi-solid mechanisms has been systematically investigated. The results indicate that the differences in stress evolution are closely related to the evolution characteristics of cathode structure and volume changes. The proposed method offers a unique view for understanding the chemo-mechanics in Li–S cells, which can be extended to different electrode materials.

 Received 3rd January 2022,
 Accepted 25th March 2022

DOI: 10.1039/d2ee00007e

rsc.li/ees

Broader context

More and more attention has been paid to new energy storage technologies represented by lithium-ion batteries. Beyond lithium-ion batteries, Li–S batteries are hopeful for next-generation energy storage. However, conventional Li–S batteries experience the dissolution–precipitation process, during which intermediate polysulfides are dissolved in the ether-based electrolyte, causing overconsumption of electrolytes and loss of active substances. Solid–solid and quasi-solid phase conversions with little liquid-phase intermediates have been proven effective to address the problems. To understand the mechanisms on a deeper level, we develop a new strategy of direct monitor on the stress evolution of Li–S cells by embedding optical fiber sensors into sulfur-based cathodes. This method is flexible and applicable to routine pouch cells, which offers a unique view for understanding the chemo-mechanics in Li–S cells. It can also be extended to different electrode materials for many other rechargeable batteries. Moreover, the research shows the potential of optical fiber sensors in battery safety issues involving monitoring parameters such as temperature and stress.

Introduction

Owing to the exceedingly high theoretical energy density ($\sim 2600 \text{ W h kg}^{-1}$) as well as the unique advantages of sulfur resources such as low-cost, non-toxic and abundant reserves,

Li–S batteries are considered as one of the most promising battery systems for future applications. Distinguished from conventional Li-ion batteries with a de-intercalation mechanism, Li–S batteries experience slightly more complex conversion reactions of sulfur and Li^+ ions.¹ The most typical Li–S cells with ether-based liquid electrolyte discharge by the “solid–liquid–solid” multi-phase conversion mechanism,² in which the pristine solid-state sulfur firstly converts to the intermediate liquid phase of lithium polysulfides (LPSS) and then to solid-phase $\text{Li}_2\text{S}_2/\text{Li}_2\text{S}$. The solvation of LPSS is the key to ensure the progress of the reaction,^{3,4} but it also brings some serious problems such as loss of active substance^{5,6} and parasitic reactions at the lithium anode.^{7,8} Since the existence of liquid-phasic polysulfides ensures the fast redox kinetics, it is difficult to reduce the amount of electrolyte. Hence, the actual energy density of the current Li–S battery technology is hard to satisfy the requirements of practical

^a State Key Laboratory of Material Processing and Die & Mould Technology, School of Materials Science and Engineering, Huazhong University of Science and Technology, Wuhan, 430074, China. E-mail: li_zhen@hust.edu.cn, huangyh@hust.edu.cn

^b School of Optical and Electronic Information, National Engineering Laboratory for Next Generation Internet Access System, Wuhan National Laboratory for Optoelectronics, Huazhong University of Science and Technology, Wuhan, 430074, China. E-mail: qzsun@mail.hust.edu.cn

† Electronic supplementary information (ESI) available. See <https://doi.org/10.1039/d2ee00007e>

‡ These authors contributed equally to this work.

application. Many efforts have been devoted to mitigating the adverse effects, such as delicate sulfur host design,^{9–12} separator modification,¹³ electrolyte regulation^{14,15} and lithium metal anode protection.¹⁶ The strategies of solid–solid conversion¹² and quasi-solid conversion,¹⁵ in which S_8 converts to Li_2S with practically no liquid-phase intermediates, can almost fundamentally avoid the series of problems caused by soluble LPSs. However, the working and failure mechanisms inside various types of Li–S cells are far more complicated and still under debate. The mechanical failure of sulfur cathodes is widely recognised as an important issue. Furthermore, the solid-phase conversion largely depends on the role of the cathode interface (CEI), but CEI may be unstable with the repeated stress variation of the cathode.¹⁷ Thus, it is necessary and urgent to find *in situ* effective characterization methods to help us understand them from the perspective of chemo-mechanics.

Lots of *in situ* characterization techniques (such as *in situ* X-ray diffraction (XRD) and *in situ* transmission electron microscopy (TEM), etc.) have been developed to improve the understandings of the potential reaction mechanism of batteries and break multiple limitations of *ex situ* characterization.^{18–22} However, most of the sophisticated *in situ* characterization instruments are expensive and the applications often tend to depend on special cell configurations that are hardly used in the regular conditions with coin cells and pouch cells. Thus, more flexible and convenient *in situ* characterization methods need to be developed to compensate for the deficiency of large *in situ* characterization methods. The development of facile monitoring methods is also necessary for a practical battery

management system (BMS) with the needs of increasingly accurate and extensive parameter measurements.²³

Temperature and stress monitoring is of great concern for battery health and hence the safety, especially for pouch cells that have practical applications. Temperature monitoring methods such as infrared thermography and radiography have contributed a lot not only for commercial pouch cells but also for fundamental studies.^{24,25} Many works also focus on cell stress monitoring by force sensing setups, most of which are based on external monitoring devices.^{26,27} In recent years, optical fiber sensors have presented great potential for *in situ* characterization of batteries owing to their strengths of lightweight, sensitivity, anti-electromagnetic interference and chemical corrosion resistance.^{28,29} The thin diameter of optical fiber sensor makes it easy to be implanted into batteries without any destruction. As a result, the internal information of cells can be collected along with the electrochemical test. Furthermore, optical fiber sensors are sensitive to both the temperature³⁰ and strain.³¹ It is possible to monitor the internal mechanical stress of the sulfur cathodes caused by continuous shrinkage and expansion of volume during the multi-phase electrochemical reactions.

In this work, we *in situ* monitor the cathode stress evolution in Li–S cells *via* optical fiber sensors. Optical fiber sensors are embedded into the sulfur-based cathodes to systematically monitor the internal chemo-mechanical stress evolution of sulfur-based cathodes under three different classic mechanisms. The obtained signals are well consistent with the structural

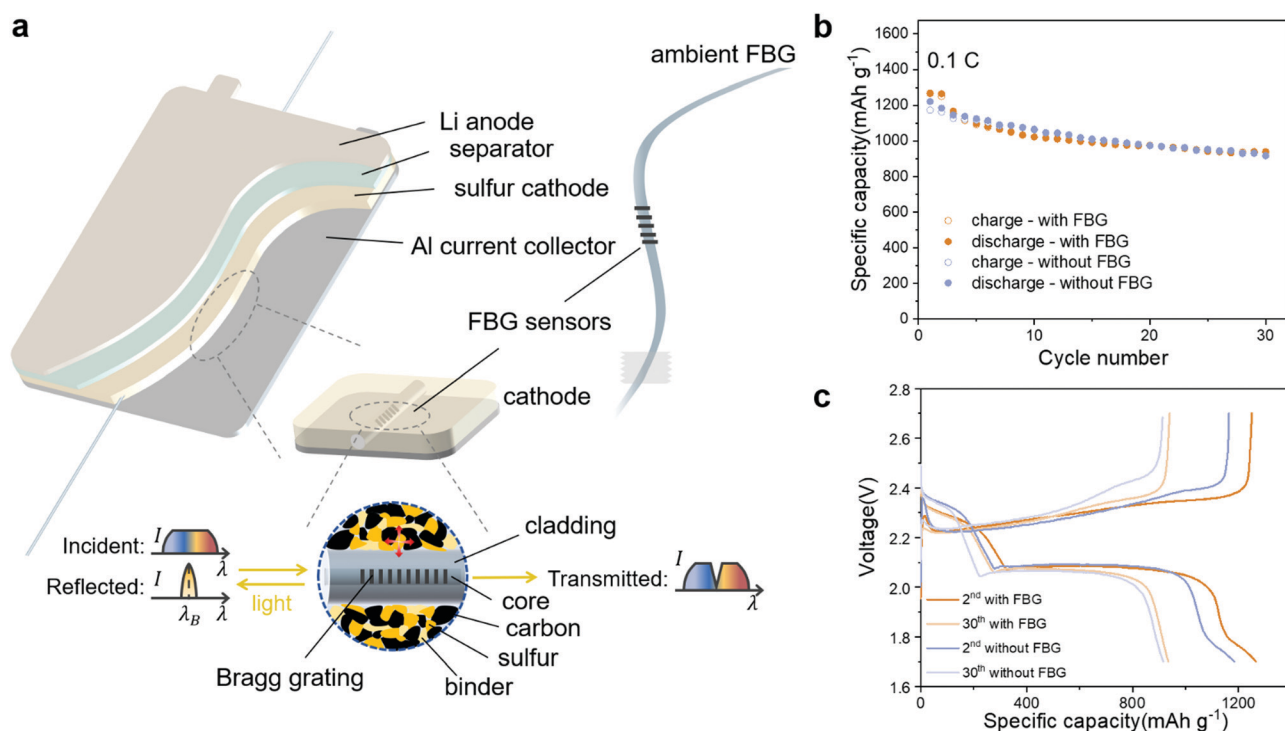


Fig. 1 Schematic of the cell embedded with FBG and corresponding electrochemical performance. (a) The schematic illustration of the structure of FBG and the Li–S pouch cell embedded with FBG. (b) The cycle performance and (c) discharge–charge curves of the Li–S pouch cell embedded with FBG and a normal cell without FBG.

evolution and volume change of the electrodes. By comparing the stress evolution of sulfur cathodes in different electrochemical conditions, it is found that, under the solid–solid mechanism, the sulfur cathode suffers from relatively more drastic stress change during the discharge–charge process. Moreover, the effect of the current density on the internal stress change of the electrode is experimentally investigated. The results give a new insight into understanding the mechanism of Li–S cells, providing a reference for the tailored design of Li–S cells from the chemo-mechanical point of view.

Results and discussion

The working principle and electrochemical immunity of FBG

There are several kinds of optical fiber sensors that can be used for temperature and strain sensing, including fiber Bragg grating (FBG),²⁸ titled fiber Bragg grating (TFBG),³² fiber Fabry–Pérot interferometer (FPI)³³ and tapered fiber.³⁴ Compared with the other optical fiber sensors, FBGs are easy to fabricate and demodulate. Moreover, the sensing performance is more stable. Therefore, FBG sensors were chosen in this work. The applied FBG consists of a periodic modulation of refractive index along the core of an optical fiber (Fig. 1a). It has a reflection/transmission effect on the light within a fixed wavelength range, and the wavelength of the reflected light satisfies formula (1):³⁵

$$\lambda_B = 2n_{\text{eff}}\Lambda \quad (1)$$

where n_{eff} refers to the core effective refractive index and Λ refers to the grating period. When an external physical quantity such as strain (ε) or temperature (T) changes, it will lead to the change in n_{eff} or Λ , and the reflection center wavelength λ_B will shift as a result. The relationship between the wavelength shifts and external parameters of temperature and strain can be simply expressed by the following formula:³⁶

$$\Delta\lambda_B = K_\varepsilon\varepsilon + K_T\Delta T \quad (2)$$

where K_T is the coefficient related to the thermal expansion coefficient and thermo-optic coefficient of the optical fiber and K_ε is the coefficient related to the elastic-optic coefficient of the optical fiber. It can be found that the FBG is a typical kind of wavelength modulated optical fiber sensor and the measured parameters can be determined by tracking the wavelength variations.

In order to realize *in situ* monitoring of the internal stress evolution in a cathode, the FBG needs to be embedded within the cathode of a single-layered stacked pouch Li–S cell. The structure of the pouch cell and FBG sensor is shown in Fig. 1a. The surrounding environment of the sensing part is also zoomed in Fig. 1a, showing the all-directional stress enforced by sulfur species. In particular, the FBG was fixed onto the aluminum foil current collector by a little of the binder. Then a layer of slurry was cast to cover the fixed FBG, embedding FBG inside the cathode materials. A schematic illustration of the process is displayed in Fig. S1 (ESI†). Hence, the cathode

materials wrapped the FBG sensor from all directions, like a coating layer. The digital images of the electrode and the cell appearance embedded with FBG is shown in Fig. S2 (ESI†). This method makes the sensing part and the substrate directly in contact for measurement, achieving the goal of *in situ* stress monitoring to the utmost extent.

It is noted that the embedded optical fiber sensor has little influence on the electrochemical behavior of the cell. To prove this point, a normal Li–S pouch cell was assembled firstly, which was composed of a ketjen black (KB)/sulfur composite cathode, ether-based electrolyte and metal lithium anode without any modification (detailed in the Methods section). Another Li–S pouch cell was embedded with FBG using the above method. The sulfur loadings of both cells were controlled at 4 mg cm^{-2} . The cycle performance of the cells is displayed on Fig. 1b, indicating little influence of the optical fiber on the capacity retention. The cell with FBG embedded delivered the initial specific capacity of 1266 mA h g^{-1} while the cell without FBG delivered the initial specific capacity of 1221 mA h g^{-1} . After 30 cycles at 0.1C, the specific capacity of the cell embedded with FBG remained at 935 mA h g^{-1} , corresponding to the overall capacity of $\sim 35 \text{ mA h}$. For the cell without FBG, the retained specific capacity was 916 mA h g^{-1} . Though the capacity retention of the cell with FBG is slightly lower than the one without FBG during the 5th to the 20th cycle, the difference is very limited and can be neglected in the research of stress evolution. From the voltage-specific capacity curves (Fig. 1c) of the 2nd and the 30th cycle, it is clearly shown that both cells remained characteristic of typical discharge dual-platforms all along, meaning that the electrochemical behavior of the Li–S cell is little impacted by the embedded FBG. In fact, the shuttle effect was not suppressed effectively with such a routine configuration, so the resulting capacity decay is on a normal degree. Furthermore, the difference in capacity delivery is within a normal range due to individual differences in cells.

In this work, the focus of our research is the stress rather than temperature, while it can be found that FBG is sensitive not only to the strain but also to the temperature from formula (1). Therefore, the influence of temperature needs to be excluded.

Since the temperature change caused by internal heat generation of a lab-level single-layered Li–S pouch cell can be negligible,^{37,38} it mainly comes from the external environment change. The influence of ambient temperature change can be removed through a difference method. In the experiment, another FBG was placed near the cell with embedded FBG to monitor the ambient temperature change, as shown in Fig. 1a. Then the wavelength shift of the embedded FBG was subtracted to the ambient FBG (Fig. S3, ESI†). It is worth noting that the FBGs were made under the same conditions and had the same temperature sensitivity. Hence, the influence of ambient temperature on wavelength shifts can be minimized to a large extent.

After removing the influence of temperature, it can be supposed that the processed FBG center wavelength shifts are mainly caused by the change in internal strain. The relationship

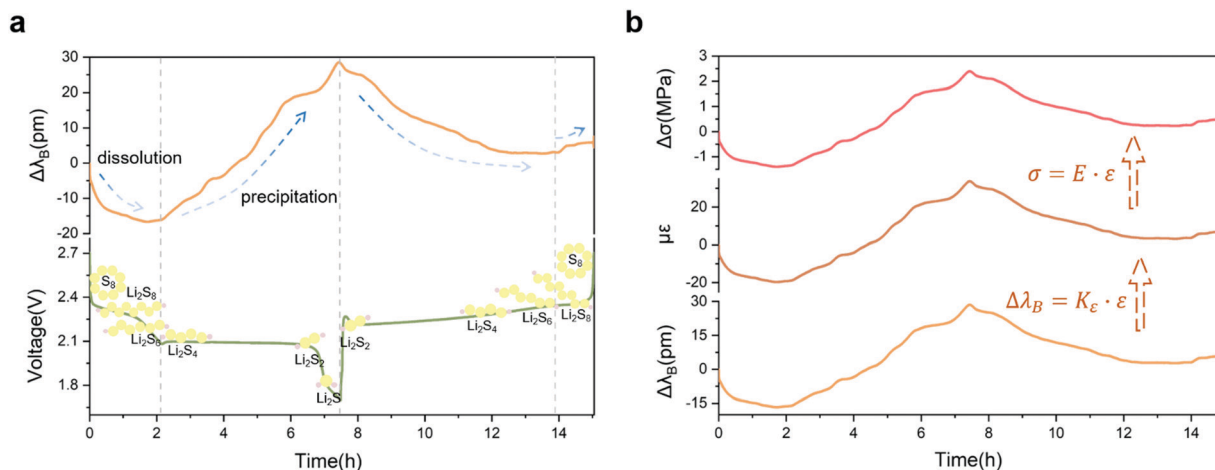


Fig. 2 The wavelength signals and conversion to the mechanical parameters. (a) One cycle of a typical discharge–charge curve of a Li–S cell and corresponding Bragg wavelength shift curve measured. (b) Schematic illustration of the conversion from wavelength shifts to stress variations.

between the wavelength change and the strain can be further simplified as eqn (3):

$$\Delta\lambda_B = K_\epsilon \epsilon \quad (3)$$

According to the experimental calibration (Fig. S4, ESI†), here the sensitivity K_ϵ equals to $0.847 \text{ pm } \mu\epsilon^{-1}$. The optical fiber can be reckoned as an ideal elastic object in a certain stress range and the stress within the elastic limit can be approximately calculated by Hooke's Law:

$$\sigma = E \cdot \epsilon \quad (4)$$

where E referring to the elastic modulus of the optic fiber is about 71 GPa. So far, the optical signal was converted into mechanical parameters successfully. The conversion process is summarized in Fig. 2b, by taking a curve of typical stress evolution in the sulfur cathode under a solid–liquid–solid mechanism as an example.

Solid–liquid–solid mechanism

Fig. 2a shows that the discharge–charge curve of a typical Li–S cell under a dissolution–precipitation mechanism consists of two discharge plateaus at about 2.3 V and 2.1 V with products at different stages marked. When the voltage reaches about 2.3 V during discharge, α -sulfur in the solid-phase is lithiated to long- and medium-chain LPSS (Li_2S_n , $n = 4, 6, 8$) dissolving in ether electrolyte. During the electrochemical reactions, the voltage drops to the long platform at 2.1 V when Li_2S_4 are gradually reduced to short-chain Li_2S_2 or Li_2S , both of which are almost insoluble in ether electrolyte and emerge as a solid-phase. After that, the sudden drop in the voltage is considered as the transformation from Li_2S_2 to Li_2S . Considering the difference in density and the number of moles between S_8 and the final discharge product Li_2S , sulfur cathodes are believed to undergo relatively large volume expansion during discharge, which brings a negative effect on the mechanical stability of electrodes.³⁹

By decoding the wavelength shift signals of the embedded FBG, it is found that the sulfur cathode operating under a solid–liquid–solid mechanism experiences a series of complex stress variations as a result of the volume change (or phase change) (Fig. 3a). At the beginning stage of discharge (region I), due to the dissolution of long-chain LPSS or the volume shrinkage, the sulfur cathode experiences the stress release and the stress variation exhibits a negative change. The stress state reaches the lowest level throughout one discharge–charge cycle at the end of region I. Then the cell discharges to region II, when the stress measured begins to increase reversely at the end of the first plateau. It is speculated to be related with the generation of solid-phase products. Subsequently, the stress increases monotonously till the end of discharge because the electrode is filled up with more and more precipitation of solid-phase $\text{Li}_2\text{S}/\text{Li}_2\text{S}_2$. The stress at the end of discharge is much higher than the initial level, proving that the sulfur cathode indeed suffers from the mechanical stress increase during discharge as a result of volume expansion. The phenomenon can also be interpreted through the scanning electron microscopy (SEM) observation (Fig. 3c and e), seeing that the sulfur/carbon composite electrode became obviously denser than the pristine ones (Fig. 3b and d). The sulfur cathode swells because of the precipitation of solid-phase products, which fills up the pores distributed in the electrode. Similarly, the charge process also experiences similar stress variation. In region III, $\text{Li}_2\text{S}/\text{Li}_2\text{S}_2$ firstly converts to soluble LPSS, causing the stress to release. After that, the production of solid-state S_8 (region IV) also causes the increase of stress in the tensile direction, but it is much smaller than that in region II. The distinction might be caused by the density and morphologic difference between S_8 and Li_2S crystalline particles. Overall, the mechanical stress inside the cathode declines during the charge process. In the charged state, the cathode becomes porous again as shown in Fig. S5 (ESI†). It is worth noting that the changing amplitude at a higher rate of 0.2C is smaller, which may be explained by two reasons: (1) the capacity decay due to the loss of active

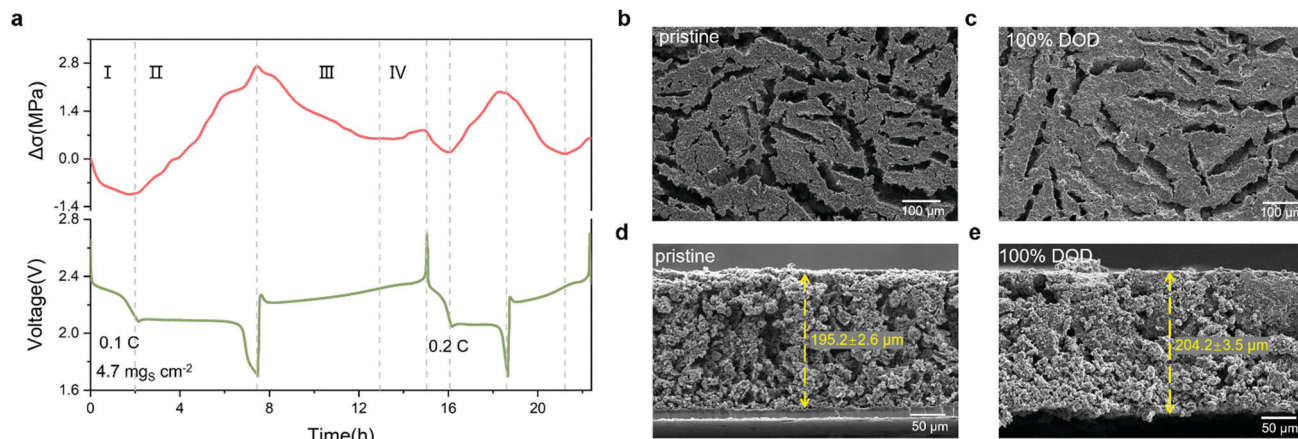


Fig. 3 Correspondence between stress and electrochemical evolution of the solid-liquid-solid mechanism. (a) The curve of stress variation obtained via embedded FBG sensors and corresponding discharge-charge curve under the solid-liquid-solid mechanism. (b-e) SEM images of KB/S electrodes from the front (b and c) and side (d and e) section, which are pristine (b and d) and fully discharged (c and e). The thickness values of the electrodes are marked as the mean with uncertainty. The sulfur loading is controlled among $4.8\text{--}5.2 \text{ mg cm}^{-2}$.

substances caused by dissolution of polysulfides, and (2) the crystallite morphology variation at different rates that the size of Li_2S crystallites is larger at a lower rate than at the higher one.⁴⁰

Solid-solid mechanism

Li-S batteries based on the solid-solid conversion mechanism features a single discharge plateau. Common strategies to realize solid-solid conversion include confining short-chain sulfur molecular (S_{2-4}) by carbon host with micropores,⁴¹ using polymer-sulfur composite materials represented by sulfurized polyacrylonitrile (noted as PANS in this article) as the cathode active substance⁴² and electrolyte regulation strategies.⁴³ Since PANS has superiority to the conventional sulfur/carbon

composite with a better rate performance and more stable cycle lifespan, herein KB/S composite cathodes were substituted for PANS cathodes and matched with carbonate-based electrolyte. Thus, the solid-phase conversion with a single plateau voltage could be achieved.

As shown in Fig. 4a, the most distinct feature of internal stress evolution in PANS materials is monotonicity, which can be rationally related to the intrinsic mechanism. During discharge, solid-phase Li_2S products gradually form accompanied by the cleavage of S-S and C-S bonds and also the coordination of Li^+ ions to the polymer backbone at the same time.⁴⁴ Since the solid-phase Li_2S products continuously deposit on the side of cathode and cause the volume expansion, the repeatable curves reveal that the internal stress keeps climbing up until the end of discharge. During the symmetrical charge process, it

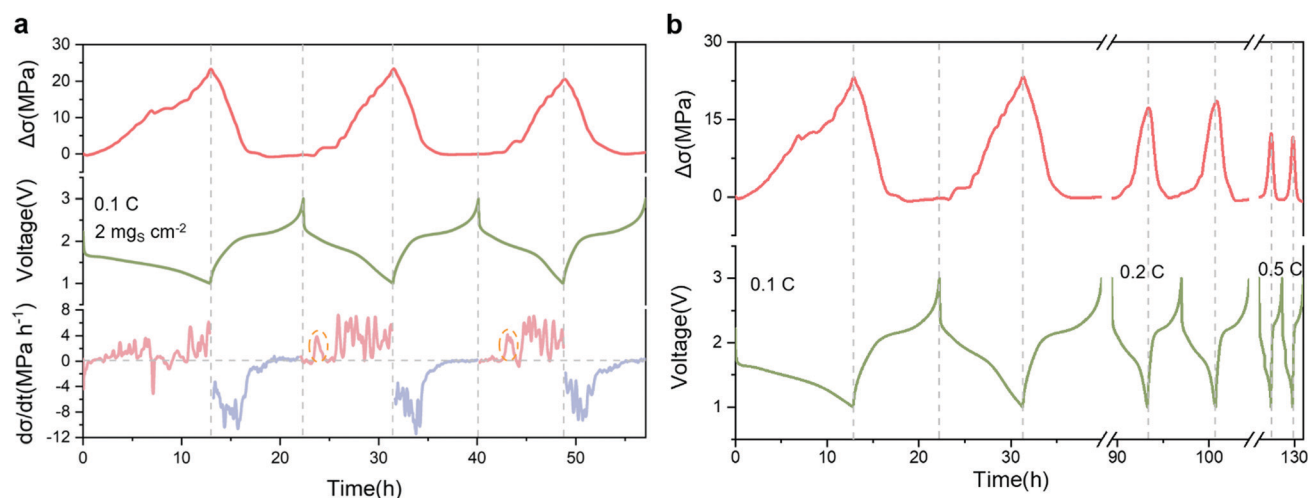


Fig. 4 Correspondence between stress and electrochemical evolution of the solid-solid mechanism. (a) The curve of stress variation obtained via embedded FBG sensors and corresponding discharge-charge curve under the solid-solid mechanism. The stress curve is in the top panel, the corresponding galvanostatic discharge-charge curve (0.1C) is in the middle panel and the differential curve of stress is in the bottom panel. (b) Discharge-charge curves under three rates and the corresponding stress curves.

drops down to the initial level, which can be explained as the reformation of S-S and C-S bonds and the reconstitution of radical PANS proposed by some viewpoints.⁴⁵ In view of the absence of the stress relief stage during discharge which is observed in the solid-liquid-solid mechanism, it is confirmed one more time that there is no liquid-phase intermediate LPSS from the new perspective of chemo-mechanics. Benefiting from the excellent rate performance of PANS, the cell at different rates continued to be tested. As shown in Fig. 4b, the 'crest' of the stress curve gradually decreases with increasing the charge-discharge rate, which is inferred to be relevant to the capacity decay and the particle size of the reaction products. The relationship between the discharge capacity and the corresponding stress variation in 15 cycles is exhibited in Fig. S6 (ESI†). It is found that they have a significantly positive correlation with a correlation coefficient of 0.893. The results reveal that FBG sensors have the potential of capacity prediction, which is of great significance in BMS.

Furthermore, the stress-time curve was differentiated for and displayed in the bottom panel of Fig. 4a. This kind of secondary treatment has been reported to be useful for deeply understanding the underlying mechanism, which can explain the structural evolution.^{46,47} Although the stress changes towards the same direction in the charge or discharge process, the slope is changeable instead of constant. The first discharge displays quite different characteristics in both the stress curve and differential curve, which may be ascribed to the irreversible reactions and unique structural evolution happening during the initial discharge. A platform approaching zero at the second half of charge is observed every cycle in the $d\sigma/dt$ curve, corresponding to the voltage platform. The platform implies that the morphologic structure has already transformed at the first half of the charge so the stress change is subtle at the second half. Notably, there is a small peak slightly after the beginning of discharge (circled in orange dashed line) except

the first one, corresponding to a 'step' reflected on the stress curve, which also exists in the $d\sigma/dt$ curve of 0.2C rate (Fig. S7, ESI†). It is deduced that the phenomenon might be connected with the nucleation-growth process of Li_2S . On the other hand, the slope of stress change at 0.2C charge-discharge (Fig. S7, ESI†) is much larger than that at 0.1C (Fig. 4a), indicative of more drastic reactions at a higher rate.

A PANS-based cell with two FBG sensors embedded and another PANS-based cell with one FBG sensor were tested to further verify the reproducibility of the results, as displayed in Fig. S8 (ESI†). The trend of the stress and the amplitudes of two cells with similar mass loading are almost the same (Fig. S8a, ESI†). For the cell with two FBGs, though the changing amplitudes of the two FBGs are different, the trends are totally the same (Fig. S8b, ESI†). The difference in amplitude is supposed to originate from the inhomogeneity of the whole electrode caused by the hand-made preparation method.

Quasi-solid mechanism

In addition to delicately designing the cathode material to suppress the shuttle effect, regulating the electrolyte to make intermediate LPSS non- or sparingly-solvated is also a compromising method. Such strategies improve the cycle stability and coulombic efficiency of Li-S cells while avoiding the complexity or high cost of cathode manufacturing. Application of high-concentrated electrolyte is a typical route. Except ether-based solvents (represented by 1,2-dimethoxy ethane (DME) and 1,3-dioxolane (DOL)) with high volatility, Nazar's group firstly reported the acetonitrile (ACN)-based electrolyte with hydro-fluoroether (HFE) co-solvent termed $[(\text{ACN})_2\text{-LiTFSI}]\text{-HFE}$, in which most solvent molecules are coordinated to Li^+ cations and few for the solvation of intermediate LPSS.¹⁵ In view of the characteristics that the intermediate polysulfides are sparingly soluble and the distinctive discharge curve, the sulfur conversion pathway is not the same neither with the

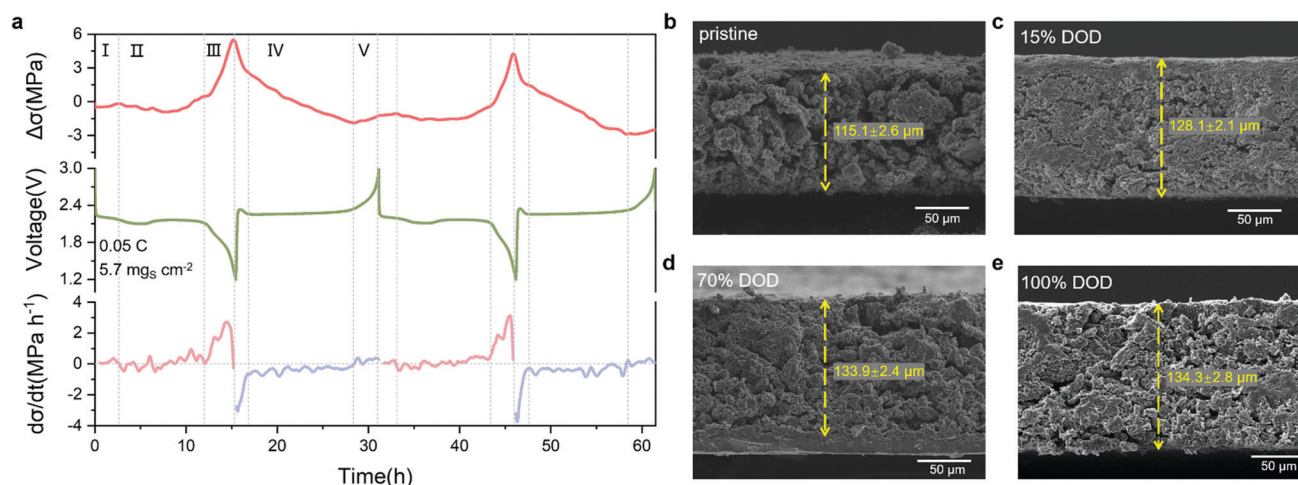


Fig. 5 Correspondence between stress and electrochemical evolution of the quasi-solid mechanism. (a) The curve of stress variation obtained via embedded FBG sensors and corresponding discharge-charge curve under the quasi-solid mechanism. (b–e) SEM cross-sectional images of the KB/S electrode which are pristine (b), 15% (c), 70% (d) and 100% (e) depth of discharge (DOD). The thickness values of the electrodes are marked as mean with uncertainty. The sulfur loading of the electrode is controlled among $3.5\text{--}4 \text{ mg cm}^{-2}$.

dissolution–precipitation conversion nor the solid-phase conversion. The reaction can be noted as a quasi-solid conversion featuring two more indistinguishable discharge voltage plateaus.⁴⁸ Unlike the solid–liquid–solid mechanism, the mobility of reactive substances under the quasi-solid mechanism rarely depends on the electrolyte but on the substance itself. This feature favors the condition of lean electrolyte but the underlying mechanism is worthy of further investigation.

The stress curve corresponding to the discharge curve is divided into five parts and the differential curve is also displayed in Fig. 5a. In region I, there is a subtle rise of stress with positive value of the slope. It can be rationally inferred to be a result of the gathering of long-chain polysulfides inside the porous cathode because their solubility and mobility in the electrolyte are largely suppressed. From the cross-sectional morphologic observation of the cathode (Fig. 5b and c), it is clear that the pores numerous distributed in the pristine electrode (Fig. 5b) have been filled at this stage (corresponding to 15% depth of discharge (DOD), Fig. 5c). The electrode becomes denser and thicker, further verifying the rationality of the increase of cathode internal stress. The cathode surface images also reveal similar features (Fig. S9a and b, ESI†). Instead of obvious trends of the stress change observed in the first two reaction mechanisms, the stress change in region II of the quasi-solid mechanism is ambiguous and smooth, which is similar to the voltage curve with a gentle slope, until the end of the voltage plateau regarded as the sign of Li_2S production. (Fig. 5a) This feature of stress change is also reflected on the $d\sigma/dt$ curve with a period of fluctuation near zero, as seen on the bottom panel of Fig. 5a. It corresponds to the transformation of long-chain LPSSs to medium- or short-chain LPSSs. As shown in Fig. 5d, this may be due to the difference of mobility between long-chain and medium- or short-chain LPSSs that the cathode got porous again. The subtle changing amplitudes of both stress and slope change reveal the relatively small volume change of the cathode until the mass production of Li_2S . In region III, there is a steep rise of both the stress change and its slope, hinting the mass and rapid conversion to the solid-phase Li_2S . It can be understood that the polysulfides solved in the electrolyte is limited, and the conversion to Li_2S immediately triggers the precipitation, leading to the drastic change. Also, the SEM image of the cross-section of the cathode (Fig. 5e) displays the thicker and denser sulfur electrode. The surface images of 70% and 100% DOD are provided in Fig. S9c and d (ESI†) as further evidence. The charge process exhibits a steep drop firstly and then a long period of gentle drop of the stress in region IV, corresponding to the oxidation from Li_2S to medium- or short-chain LPSSs first, and subsequently the transformation from medium-chain LPSSs to long-chain LPSSs. At the last stage of charge, namely region V, the stress rebounds a little, which may represent the precipitation of solid-phase S_8 .

Comparison of the three mechanisms

One representative cycle of the stress evolution curves under three reaction mechanisms of Li–S cells was extracted respectively in Fig. 6 with the horizontal axis normalized. A conclusion can be simply drawn that in sulfur-based cathodes of Li–S cells, the stress

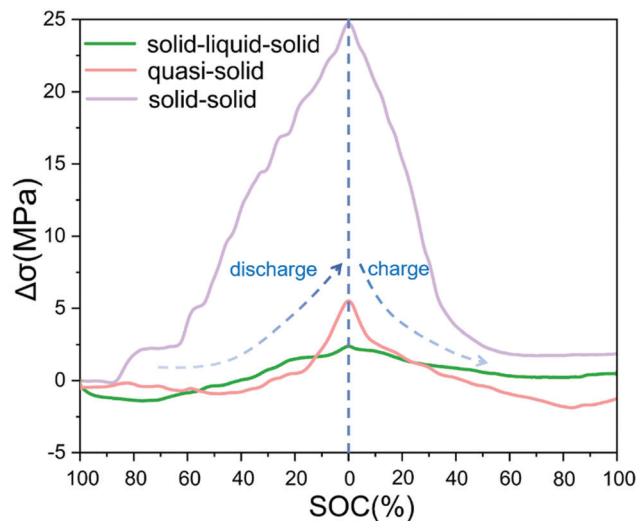


Fig. 6 Comparison of stress curves under the three mechanisms during one complete discharge–charge cycle.

is concentrated during the discharge process while it is released during the charge process. The difference in the law of stress change among the three mechanisms is also clear at a glance from Fig. 6. The sulfur cathode shows the highest stress change under the solid–solid mechanism, and the lowest under the solid–liquid–solid mechanism during charge/discharge processes. This result brings us new enlightenment in understanding Li–S batteries. It can be explained by chemical and physical consideration from three aspects: (1) in addition to solid–solid conversion, liquid-phase intermediate products exist during the electrochemical reactions under the other two mechanisms, which may help to avoid the rapid stress concentration caused by the precipitation of solid-phase Li_2S and plays a role in buffering the mechanical stress; (2) to realize the solid–solid conversion, PANS can be adopted as the active material instead of the porous carbon/sulfur composite. As a result, the porosity in the cathode is greatly reduced, which can be proven by the SEM image (Fig. S10, ESI†) and porosity calculations. The porosity of the PANS cathode is about 60%, while the KB/S cathode in this work is about 80%. The calculation process is described in the Methods section. Furthermore, SEM images show that KB/S particles are smaller in size than PANS particles (Fig. S11, ESI†). The difference in particle size may also have influence the stress release and uptake, for the diffusion theory demonstrates that the strain dissipates more quickly in the particles with smaller dimensions.⁴⁹ Hence, the spatial redundancy which can accommodate the deposition of solid-phase products is greatly reduced and the transformation to Li_2S is much easier to lead to the immediate rise of stress; (3) since the elastic modulus of the substrate could have great influence upon the stress transfer between the substrate and the embedded FBG, the elastic modulus of PANS and KB/S substrate materials were measured through the atomic force microscopy (AFM) characterization. It is found from Fig. S12 (ESI†) that the elastic modulus of PANS is larger than KB/S on average, which favors the stress transfer and may cause the higher value of stress monitored. It must be

mentioned that the electrochemical reactions take place all along the discharge/charge process, so the environment in which the embedded FBG is located can be largely changeable. However, it's hard to monitor the properties of substrate at every stage of the phase or substance conversion in order to explain from a more precise and rigorous perspective. Our analysis and experimental results are credible to provide a basic opinion and understanding.

Conclusions

We have succeeded in *in situ* monitoring the internal stress evolution of sulfur-based cathodes in a Li-S cell *via* flexible FBG sensors. The stress evolution curve corresponds well to the acknowledged phasic changing process occurring during the electrochemical reactions under three typical mechanisms of Li-S cells. From the results, the stress evolution under the solid-solid mechanism based on the PANS cathode material is more drastic than the others both in rate and amplitude, while the KB/S cathode under the solid-liquid-solid mechanism undergoes the minimal mechanical change. The severity of the change is related to not only the degree of volume change but also the nature of the materials. These results provide brand-new insight and consideration on the assessment of the mechanisms in Li-S cells and guide the future work in the Li-S battery field from the perspective of chemo-mechanical stress. The solid-solid mechanism and quasi-solid mechanism though have superiority over the solid-liquid-solid mechanism in improving battery performance, and the potential mechanical stress problems should be taken into consideration. Although there are still details remaining that have not been fully explained, the developed method can be a reference assessment standard for judging a new-type Li-S battery system and help understand the intrinsic conversion mechanism of other newly developed Li-S electrode materials or electrolytes.

Methods

Preparation of KB/S and PANS materials

The synthesis of KB/S used in the research of solid-liquid-solid mechanism and quasi-solid mechanism was based on the conventional melt-diffusion method that 70 wt% KB/S mixture is processed at 155 °C for 12 h. PANS materials were synthesized by heating the mixture of sulfur and polyacrylonitrile (PAN) ($M_w = 150\,000\text{ g mol}^{-1}$) with a mass ratio of 2:1 at 350 °C for 6 h under a flowing Ar atmosphere. The process was repeated again to get rid of the extra sulfur by locating the sample in a porcelain boat. The S content is 41.5 wt% determined by element analysis.

Fabrication of FBG sensors

The FBG sensors were inscribed with a pulsed 248 nm UV KrF laser together with a phase mask. The 248 nm KrF excimer laser (LightMachinery-IPX700) has a beam size of 10×20 (mm), with a maximum pulse energy of 300 mJ, and maximum repetition rate of 25 Hz. Firstly, a conventional single-mode fiber (Corning SMF-28) was loaded in hydrogen (13 Mpa and 80 °C for 10 days)

to increase the photosensitivity. Then it was fixed using a fiber holder and the laser beam was focused by using a cylindrical lens with a focal length of 30 mm, passed through a shaping slit (5 mm) and a uniform phase mask (Ibsen Photonics, grating period: 1071.2 nm) onto the SMF to fabricate FBG. The reflective spectra of fabricated FBGs were monitored using an optical analyzer (Yokogawa-AQ6375B) to determine their effects.

Preparation of a positive electrode embedded with FBG

The aluminum foil current collector was tailored into a square slice and was fixed on a board. Then a FBG was fixed onto the aluminum foil by a LA133 binder. The coating of the fiber on the grating section was peeled off. Then the cathode slurry was cast on the current collector, covering the FBG. The KB/S cathode slurry consists of KB/S powder and LA133 binder with a mass ratio of 9:1. The PANS cathode slurry consists of PANS powder, LA133 binder and a carbon nanotube (CNT) with a mass ratio of 8:1:1. The KB/S cathode was dried using a freeze-drying method and the PANS cathode was dried in a 70 °C drying oven.

Porosity calculation

For the porosity calculation (noted as p), the basic formula is as follows:⁵⁰

$$p = \frac{V_{\text{cathode}} - V_{\text{material}} - V_{\text{binder}} - V_{\text{conductive}}}{V_{\text{cathode}}} \quad (5)$$

where V_{cathode} , V_{material} , V_{binder} and $V_{\text{conductive}}$ are the volumes of the whole cathode, active material, binder and conductive carbon, respectively. V_{cathode} can be obtained from the geometry size of the cathode, and the sum of the latter three is the dense volume. Herein the coin cell cathodes with an area of 0.5 cm^2 are taken as examples. For the KB/S cathode with sulfur loading of 5 mg cm^{-2} , p is $\sim 80\%$. For the PANS cathode with sulfur loading of 2 mg cm^{-2} , p is $\sim 60\%$. The parameters involved are available in Table S1 (ESI[†]).

Electrochemical measurement

Electrochemical tests were performed by using single-layered stacked pouch cells assembled in an argon-filled glove box. A Celgard 2400 membrane tailored into a square slightly larger than the electrode was used as the separator. The anode is a piece of metal lithium foil ($\sim 100\text{ }\mu\text{m}$). The electrolyte used in the research of the solid-liquid-solid mechanism contains 1 M bis (trifluoromethane-sulfonyl) imide lithium LiTFSI in 1:1 v/v DOL:DME with 2% lithium nitrate (LiNO_3). The electrolyte used in the research of the solid-solid mechanism contains 1 M lithium hexafluorophosphate (LiPF_6) in 1:1 v/v ethylene carbonate (EC)/diethyl carbonate (DEC) with 5 wt% FEC. The electrolyte we used in the research of the quasi-solid mechanism was homemade and consists of 3.7 M LiTFSI in acetonitrile (ACN) with 1,1,2,2-Tetra uoroethyl 2,2,3,3-tetrauoropropyl ether (HFE) (1:1 v/v).¹⁵ The electrolyte/sulfur ratio (E/S) is around $20\text{ }\mu\text{L mg S}^{-1}$. The galvanostatic charge-discharge processes were conducted on a NEWARE CT-9040 battery test system.

Published on 25 March 2022. Downloaded by Xian Jiaotong University on 6/6/2023 2:12:38 AM.

- 26 J. Cannarella and C. B. Arnold, *J. Power Sources*, 2014, **245**, 745–751.
- 27 R. Fu, M. Xiao and S.-Y. Choe, *J. Power Sources*, 2013, **224**, 211–224.
- 28 J. Huang, L. Alberio Blanquer, J. Bonafacino, E. R. Logan, D. Alves Dalla Corte, C. Delacourt, B. M. Gallant, S. T. Boles, J. R. Dahn, H. Y. Tam and J. M. Tarascon, *Nat. Energy*, 2020, **5**, 674–683.
- 29 L. W. Sommer, A. Raghavan, P. Kiesel, B. Saha, J. Schwartz, A. Lochbaum, A. Ganguli, C. J. Bae and M. Alamgir, *J. Electrochem. Soc.*, 2015, **162**, A2664–A2669.
- 30 T. He, Y. Ran, T. Liu, C. Fan, W. Zhou, Z. Yan, D. Liu and Q. Sun, *IEEE Photonics J.*, 2019, **11**(6), 1–11.
- 31 T. Liu, H. Li, T. He, C. Fan, Z. Yan, D. Liu and Q. Sun, *Opto-Electron. Adv.*, 2021, **4**(5), 200037.
- 32 J. Huang, X. Han, F. Liu, C. Gervillie, L. A. Blanquer, T. Guo and J.-M. Tarascon, *Energy Environ. Sci.*, 2021, 6464–6475, DOI: [10.1039/d1ee02186a](https://doi.org/10.1039/d1ee02186a).
- 33 S. Pevec and D. Donlagic, *Appl. Opt.*, 2012, **51**(19), 4536–4541.
- 34 J. L. Kou, J. Feng, L. Ye, F. Xu and Y. Q. Lu, *Opt. Express*, 2010, **18**, 14245–14250.
- 35 K. O. Hill and G. Meltz, *J. Lightwave Technol.*, 1997, **15**, 1263–1276.
- 36 R. P. DePaula, W. W. Morey, E. Udd, G. Meltz and W. H. Glenn, presented in part at the Proc. SPIE, 1990.
- 37 D. Bernardi, E. Pawlikowski and J. Newman, *J. Electrochem. Soc.*, 1985, **132**, 5–12.
- 38 C. Heubner, M. Schneider, C. Lämmel and A. Michaelis, *Electrochim. Acta*, 2015, **186**, 404–412.
- 39 X. He, J. Ren, L. Wang, W. Pu, C. Jiang and C. Wan, *J. Power Sources*, 2009, **190**, 154–156.
- 40 S. Waluś, G. Offer, I. Hunt, Y. Patel, T. Stockley, J. Williams and R. Purkayastha, *Energy Storage Mater.*, 2018, **10**, 233–245.
- 41 C. Fu, M. B. Oviedo, Y. Zhu, A. von Wald Cresce, K. Xu, G. Li, M. E. Itkis, R. C. Haddon, M. Chi, Y. Han, B. M. Wong and J. Guo, *ACS Nano*, 2018, **12**, 9775–9784.
- 42 J. Wang, J. Yang, C. Wan, K. Du, J. Xie and N. Xu, *Adv. Funct. Mater.*, 2003, **13**, 487–492.
- 43 G. Xu, H. Sun, C. Luo, L. Estevez, M. Zhuang, H. Gao, R. Amine, H. Wang, X. Zhang, C. Sun, Y. Liu, Y. Ren, S. M. Heald, C. Wang, Z. Chen and K. Amine, *Adv. Energy Mater.*, 2019, **9**, 1802235.
- 44 X. Wang, Y. Qian, L. Wang, H. Yang, H. Li, Y. Zhao and T. Liu, *Adv. Funct. Mater.*, 2019, **29**, 1902929.
- 45 W. Wang, Z. Cao, G. A. Elia, Y. Wu, W. Wahyudi, E. Abou Hamad, A. H. Emwas, L. Cavallo, L. J. Li and J. Ming, *ACS Energy Lett.*, 2018, **3**, 2899–2907.
- 46 S. Jun, Y. J. Nam, H. Kwak, K. T. Kim, D. Y. Oh and Y. S. Jung, *Adv. Funct. Mater.*, 2020, **30**, 2002535.
- 47 S. Y. Han, C. Lee, J. A. Lewis, D. Yeh, Y. Liu, H. W. Lee and M. T. McDowell, *Joule*, 2021, **5**, 1–16.
- 48 Q. Pang, A. Shyamsunder, B. Narayanan, C. Y. Kwok, L. A. Curtiss and L. F. Nazar, *Nat. Energy*, 2018, **3**, 783–791.
- 49 J. Graetz, C. C. Ahn, R. Yazami and B. Fultz, *Electrochem. Solid-State Lett.*, 2003, **6**, A194–A197.
- 50 N. Kang, Y. Lin, L. Yang, D. Lu, J. Xiao, Y. Qi and M. Cai, *Nat. Commun.*, 2019, **10**, 4597.